

Scalar absorption beyond geometric optics in Klein–Gordon-separable Johannsen black hole spacetimes

Jining Tang^{1*} Yang Huang^{2†} Hongsheng Zhang^{2‡}

School of Physics and Technology, University of Jinan,
336 West Road of Nan Xinzhuang, Jinan, Shandong 250022, China

May 28, 2026

Abstract

Johannsen metric is a natural and significant generalization of the Kerr metric, representing the most general stationary, axisymmetric spacetime that preserves the Carter constant of motion. The theoretical status furnishes a powerful, systematic framework for strong-field tests of the no-hair theorem and for investigations of deviations from Kerr black-hole geometries. We formulate massless scalar plane-wave absorption in a Klein–Gordon-separable subclass of Johannsen spacetimes. In the asymptotically flat Johannsen metric, we impose Klein–Gordon separability, derive the separated angular and radial equations, and build a partial wave framework for the leading deformation sectors $A_1(r)$, $A_2(r)$, and $A_5(r)$. The resulting description separates deformations that change the radial size function $X(r)$ from those that enter only the radial kinetic term. The former modify the low-frequency area law, the high-frequency null-capture cross section, and the finite-frequency absorption spectra, whereas a pure A_5 deformation leaves the leading null-capture observable unchanged while remaining detectable in wave propagation. We further examine off-axis incidence, co-/counter-rotating contributions, and superradiant modes, where changes in $X(r_+)$ shift the horizon angular velocity and hence the superradiant threshold. Our results identify finite-frequency absorption as a wave-optics diagnostic that can probe radial propagation sectors inaccessible to both the area law and null geodesic capture observables, offering a new tool for strong-field tests of black hole geometry.

Keywords: black holes; scalar fields; absorption cross section; Johannsen metric; null geodesics

PACS/MS/Subject classification: 04.70.-s; 04.30.Nk; 04.50.Kd

I Introduction

The Kerr solution is the standard exterior geometry of an isolated rotating black hole in general relativity [1, 2]. Strong-field observations now test this assumption directly through

*Electronic address: aishiker1998@gmail.com

†Electronic address: sps_Huangy@ujn.edu.cn

‡Electronic address: sps_zhanghs@ujn.edu.cn (contact author)

gravitational waves, horizon-scale imaging, and related probes of compact object dynamics [3–5]. A useful theoretical strategy is therefore to work with Kerr-type metrics that preserve enough symmetry for observable calculations, while introducing controlled deviations that can be connected either to phenomenology or to exact alternatives to Kerr. We follow standard general relativity and black hole conventions as presented in classic treatments of the subject [6–9].

Parametrized rotating metrics provide such a framework. The original Johannsen–Psaltis construction was designed for strong-field tests of the no-hair conjecture, but generic deformations may introduce pathologies or lose integrability at large dimensionless spin [10, 11]. The Johannsen metric used here is more suitable for analytic and numerical absorption calculations because it is regular outside the event horizon in the allowed parameter domain, admits a Carter-type constant, and packages deviations into radial functions that can be compared with known black hole metrics for special parameter choices [12]. Closely related work on parametrized Kerr-type geometries clarifies the role of asymptotic flatness, coordinate choices, hidden symmetries, and separability in restricting admissible deviations [13, 14].

The distinction between geodesic separability and wave separability is central to the present problem. Hamilton–Jacobi separability makes photon orbits and geometric observables tractable, but scalar absorption requires the Klein–Gordon (KG) equation to separate in the same coordinates. Konoplya, Stuchlík, and Zhidenko constructed a broad axisymmetric class admitting both Hamilton–Jacobi and Klein–Gordon separability, while Chen and Chen derived analogous constraints for rotating spacetimes generated through the Newman–Janis algorithm [15, 16]. Shadow calculations in general rotating spacetimes and in Johannsen-type geometries further show that null geodesic observables probe only selected combinations of the metric functions [17–20]. This motivates asking which deformation sectors remain visible when one goes beyond geometric optics.

Black-hole absorption supplies a complementary probe. The classic scalar wave problem ranges from low energy absorption by small black holes to Schwarzschild absorption spectra and Hawking emission greybody factors [21–23]. In Kerr, the separable wave equations, superradiant amplification, and partial wave absorption formalism were developed through the Teukolsky–Starobinsky–Press framework and later numerical studies [24–28]. Subsequent work extended the comparison to electromagnetic and gravitational waves, incidence-angle dependence, and co-/counter-rotating mode decompositions [29–31].

Different frequency regimes isolate different aspects of the geometry. In the low-frequency regime, the massless scalar absorption cross section approaches the horizon area for broad classes of stationary black holes [32–34]. In the high-frequency regime, the cross section approaches the geometric capture area, with oscillatory corrections described by complex angular momentum, Regge pole, and sinc approximations tied to unstable null orbits [35–39]. Finite-frequency spectra occupy the intermediate regime in which the full radial wave barrier matters. This is already visible in Kerr–Newman, tidal-charge, regular black-hole, conformally related, and dilatonic backgrounds, where partial-wave absorption and scattering can distinguish structures that are degenerate in one of the limiting regimes [40–45]. Full-wave studies of charged dilatonic black holes, for example, combine partial-wave and Regge-pole methods with classical-geodesic and glory approximations [45]. More recently, scalar absorption and scattering by Frolov regular

black holes showed that Frolov, Reissner–Nordström, and Hayward spectra can become nearly degenerate when the relevant critical or glory impact parameters are matched [46]. These results motivate the present question in a rotating parametrized spacetime: which deformation sectors remain visible to finite-frequency waves after the low-frequency area law and high-frequency null-capture limit have been fixed?

In this work we formulate the finite-frequency massless scalar plane-wave absorption problem for a Klein–Gordon-separable Johannsen subclass and use it to compare the leading $A_1(r)$, $A_2(r)$, and $A_5(r)$ deformation sectors. The central question is whether finite-frequency absorption can probe radial propagation sectors that are invisible to both the low-frequency area law and the high-frequency null capture limit. The paper is organized as follows. Section II defines the metric subclass and the separability restrictions. Section III derives the separated scalar equations and the radial boundary-value problem. Section IV discusses the absorption cross section and its low- and high-frequency limits. Section V presents the finite-frequency spectra, incidence-angle dependence, and superradiant mode behavior. Section VI summarizes the physical interpretation and possible extensions. Throughout the paper we use geometrized units $G = c = \hbar = 1$ and the metric signature $(-, +, +, +)$.

II Klein–Gordon–Separable Johannsen Spacetimes

The Johannsen metric is a parametrized deformation of Kerr designed to keep stationarity, axisymmetry, asymptotic flatness, and three independent geodesic constants of motion while introducing strong field deviations from the Kerr geometry [12]. In this section we keep the logical order explicit. We first display the asymptotically flat Johannsen geometry, then impose Klein–Gordon separability, and only afterwards discuss the additional weak field restrictions used in the canonical parametrization. This separation of assumptions is important because the KG-separable subclass and the parametrized post-Newtonian (PPN) compatible subclass need not coincide a priori. In Boyer–Lindquist coordinates the Kerr seed is

$$ds_{\text{K}}^2 = - \left(1 - \frac{2Mr}{\Sigma}\right) dt^2 - \frac{4Mar \sin^2 \theta}{\Sigma} dt d\phi + \frac{\Sigma}{\Delta} dr^2 + \Sigma d\theta^2 + \frac{[(r^2 + a^2)^2 - a^2 \Delta \sin^2 \theta] \sin^2 \theta}{\Sigma} d\phi^2, \quad (1)$$

where

$$\Delta = r^2 - 2Mr + a^2, \quad \Sigma = r^2 + a^2 \cos^2 \theta. \quad (2)$$

Here M is the black hole mass and $a = J/M$ is the Kerr spin parameter, i.e., the specific angular momentum. The dimensionless spin is $a/M = J/M^2$. Johannsen’s starting point is a deformation of the contravariant Kerr operator by radial functions A_1, A_2, A_5, f and angular functions A_3, A_4, A_6, g ,

$$\tilde{\Sigma} g^{\alpha\beta} \frac{\partial}{\partial x^\alpha} \frac{\partial}{\partial x^\beta} = - \frac{\left[(r^2 + a^2) A_1(r) \frac{\partial}{\partial t} + a A_2(r) \frac{\partial}{\partial \phi} \right]^2}{\Delta} + \frac{\left[A_3(\theta) \frac{\partial}{\partial \phi} + a \sin^2 \theta A_4(\theta) \frac{\partial}{\partial t} \right]^2}{\sin^2 \theta} + \Delta A_5(r) \frac{\partial^2}{\partial r^2} + A_6(\theta) \frac{\partial^2}{\partial \theta^2}, \quad (3)$$

with

$$\tilde{\Sigma} = \Sigma + f(r) + g(\theta). \quad (4)$$

The separable ansatz is imposed at the Hamilton–Jacobi level. For a test particle of rest mass m_0 ,

$$-\frac{\partial S}{\partial \tau} = \frac{1}{2} g^{\alpha\beta} \frac{\partial S}{\partial x^\alpha} \frac{\partial S}{\partial x^\beta}, \quad (5)$$

and

$$S = \frac{1}{2} m_0^2 \tau - Et + L_z \phi + S_r(r) + S_\theta(\theta). \quad (6)$$

Substitution gives

$$\begin{aligned} -m_0^2 = & -\frac{[-(r^2 + a^2)A_1(r)E + aA_2(r)L_z]^2}{\Delta \tilde{\Sigma}} + \frac{[A_3(\theta)L_z - aA_4(\theta)E \sin^2 \theta]^2}{\tilde{\Sigma} \sin^2 \theta} \\ & + \frac{\Delta A_5(r)}{\tilde{\Sigma}} \left(\frac{dS_r}{dr} \right)^2 + \frac{A_6(\theta)}{\tilde{\Sigma}} \left(\frac{dS_\theta}{d\theta} \right)^2. \end{aligned} \quad (7)$$

After multiplying by $\tilde{\Sigma}$ the radial and angular terms separate. The separation constant C may be written equivalently as

$$C = \frac{[-(r^2 + a^2)A_1(r)E + aA_2(r)L_z]^2}{\Delta} - m_0^2 [r^2 + f(r)] - \Delta A_5(r) \left(\frac{dS_r}{dr} \right)^2, \quad (8)$$

$$C = \frac{[A_3(\theta)L_z - aA_4(\theta)E \sin^2 \theta]^2}{\sin^2 \theta} + m_0^2 [a^2 \cos^2 \theta + g(\theta)] + A_6(\theta) \left(\frac{dS_\theta}{d\theta} \right)^2. \quad (9)$$

The Carter-type constant is

$$Q = C - (L_z - aE)^2. \quad (10)$$

Following the convention discussed by de Felice and Preti [47], we also define

$$\Lambda = C + 2aEL_z - m_0^2 a^2. \quad (11)$$

This quantity reduces to the ordinary squared angular momentum in the asymptotically flat, nonrotating limit. We use the geodesic construction only to identify the metric class; the absorption calculation below is based on the Klein–Gordon equation.

The radial deviation functions are expanded as

$$A_i(r) = \sum_{n=0}^{\infty} \alpha_{in} \left(\frac{M}{r} \right)^n, \quad i = 1, 2, 5, \quad (12)$$

while

$$f(r) = \sum_{n=0}^{\infty} \epsilon_n \frac{M^n}{r^{n-2}}, \quad g(\theta) = M^2 \sum_{k,l=0}^{\infty} \gamma_{kl} \sin^k \theta \cos^l \theta, \quad \gamma_{00} = 0. \quad (13)$$

Asymptotic flatness fixes

$$\alpha_{10} = \alpha_{20} = \alpha_{50} = 1, \quad \epsilon_0 = \epsilon_1 = 0, \quad A_3(\theta) = A_4(\theta) = A_6(\theta) = 1. \quad (14)$$

If the parameters M and a are further required to coincide with the physical mass and Kerr spin

parameter in the canonical Johannsen normalization, then

$$\alpha_{11} = \alpha_{21} = \alpha_{51} = 0. \quad (15)$$

With these restrictions the nonzero covariant components take the compact form

$$\mathcal{D}(r, \theta) = (r^2 + a^2)A_1(r) - a^2A_2(r) \sin^2 \theta. \quad (16)$$

$$g_{tt} = -\frac{\tilde{\Sigma} [\Delta - a^2A_2(r)^2 \sin^2 \theta]}{\mathcal{D}^2}, \quad (17)$$

$$g_{t\phi} = -\frac{a [(r^2 + a^2)A_1(r)A_2(r) - \Delta] \tilde{\Sigma} \sin^2 \theta}{\mathcal{D}^2}, \quad (18)$$

$$g_{rr} = \frac{\tilde{\Sigma}}{\Delta A_5(r)}, \quad g_{\theta\theta} = \tilde{\Sigma}, \quad (19)$$

$$g_{\phi\phi} = \frac{\tilde{\Sigma} \sin^2 \theta [(r^2 + a^2)^2 A_1(r)^2 - a^2 \Delta \sin^2 \theta]}{\mathcal{D}^2}. \quad (20)$$

Equations (17)–(20) reduce to Kerr when all deviations vanish.

We next impose separability of a massive scalar field. Let

$$(\square - \mu^2) \Phi = 0, \quad \Phi = e^{-i\omega t} e^{im\phi} \psi(r, \theta), \quad (21)$$

where μ is the scalar field mass. Substituting Eq. (21) into the asymptotically flat Johannsen metric and multiplying the resulting equation by $\tilde{\Sigma}^2/\mathcal{D}$ gives

$$\begin{aligned} & \sqrt{A_5} \frac{\partial}{\partial r} \left[\Delta \sqrt{A_5} \frac{\tilde{\Sigma}}{\mathcal{D}} \frac{\partial \psi}{\partial r} \right] + \frac{1}{\sin \theta} \frac{\partial}{\partial \theta} \left[\sin \theta \frac{\tilde{\Sigma}}{\mathcal{D}} \frac{\partial \psi}{\partial \theta} \right] \\ & + \frac{\tilde{\Sigma}}{\mathcal{D} \Delta} \left\{ [\omega(r^2 + a^2)A_1(r) - amA_2(r)]^2 - \Delta \left(a\omega \sin \theta - \frac{m}{\sin \theta} \right)^2 \right\} \psi - \mu^2 \frac{\tilde{\Sigma}^2}{\mathcal{D}} \psi = 0. \end{aligned} \quad (22)$$

This form motivates the definition

$$Y(r, \theta) \equiv \frac{\tilde{\Sigma}}{\mathcal{D}}. \quad (23)$$

It is also convenient to set

$$\mathcal{N}(r, \theta) = [\omega(r^2 + a^2)A_1(r) - amA_2(r)]^2 - \Delta \left(a\omega \sin \theta - \frac{m}{\sin \theta} \right)^2. \quad (24)$$

Then Eq. (22) becomes

$$\sqrt{A_5} \partial_r \left(\Delta \sqrt{A_5} Y \partial_r \psi \right) + \frac{1}{\sin \theta} \partial_\theta \left(\sin \theta Y \partial_\theta \psi \right) + Y \frac{\mathcal{N}}{\Delta} \psi - \mu^2 \tilde{\Sigma} Y \psi = 0. \quad (25)$$

After division by $Y\psi$, the mass term is $-\mu^2 \tilde{\Sigma}$ and remains additively separable. The nontrivial obstruction is therefore the factor Y . With $y = \cos \theta$,

$$Y(r, y) = \frac{r^2 + f(r) + a^2 y^2 + g(y)}{(r^2 + a^2)A_1(r) - a^2 A_2(r) + a^2 A_2(r) y^2}. \quad (26)$$

Separation requires $Y(r, y) = Y_r(r)Y_y(y)$, equivalently $\frac{\partial^2}{\partial r \partial y} \ln Y = 0$. For nonzero spin parameter this condition forces $g(y)$ to be independent of y , so $g(\theta) = g_0$ is a constant. Since $\tilde{\Sigma}$ depends on $f(r)$ and $g(\theta)$ only through the combination $f(r) + g(\theta)$, this constant can be absorbed into the constant part of $f(r)$. With the Johannsen convention $\gamma_{00} = 0$, we choose the representative

$$g(\theta) = 0, \quad (27)$$

and the remaining radial functions must satisfy

$$(r^2 + a^2)A_1(r) = [r^2 + a^2 + f(r)]A_2(r). \quad (28)$$

Equivalently,

$$f(r) = \frac{(r^2 + a^2)A_1(r)}{A_2(r)} - (r^2 + a^2). \quad (29)$$

Combining the KG separability constraint in Eq. (28) with the power series definitions of A_1 , A_2 , and f gives, for the first two nontrivial coefficients,

$$\alpha_{12} = \epsilon_2 + \alpha_{22}, \quad \alpha_{13} = \epsilon_3 + \alpha_{23}. \quad (30)$$

This KG-separable Johannsen subclass is a special form of the separable three function metric of Konoplya, Stuchlík, and Zhidenko [15]. The comparison is useful mainly as a structural check: it shows which Johannsen functions control the redshift sector, the effective radial size, and the radial kinetic term in a general separable rotating metric. If that metric is written in terms of $R_M(r)$, $R_\Sigma(r)$, and $R_B(r)$, the corresponding Johannsen functions obey

$$A_2(r) = \left[\frac{\Delta}{r^2 R_\Sigma(r) + a^2 - r R_M(r)} \right]^{1/2}, \quad A_1(r) = \frac{r^2 R_\Sigma(r) + a^2}{r^2 + a^2} A_2(r), \quad (31)$$

$$A_5(r) = \frac{1}{R_B(r)^2 A_2(r)^2}, \quad f(r) = r^2 [R_\Sigma(r) - 1]. \quad (32)$$

Large radius expansions of these relations connect the Johannsen coefficients to several exact or phenomenological rotating metrics. The following identifications are matches at the level of coefficients in the asymptotic expansion; when a target solution has long range charge terms, the mapping should not be read as membership in the final working subclass. For the Kerr–Newman solution [48],

$$\alpha_{12} = \alpha_{22} = -\frac{Q^2}{2M^2}, \quad \alpha_{13} = \alpha_{23} = -\frac{Q^2}{M^2}, \quad \alpha_{52} = \frac{Q^2}{M^2}, \quad (33)$$

where Q denotes the electric charge. For the modified Kerr metric of Ref. [49],

$$\alpha_{13} = \alpha_{23} = \frac{\eta}{2M^3}, \quad \alpha_{53} = -\frac{\eta}{M^3}, \quad \alpha_{22} = \alpha_{52} = 0. \quad (34)$$

For the Kerr–Sen solution [50], the leading nonzero coefficients are

$$\epsilon_1 = \frac{2b}{M}, \quad \alpha_{11} = \frac{b}{M}, \quad \alpha_{21} = -\frac{b}{M}, \quad \alpha_{51} = \frac{2b}{M}, \quad (35)$$

$$\alpha_{12} = -\frac{2b}{M} - \frac{b^2}{2M^2}, \quad \alpha_{22} = -\frac{2b}{M} + \frac{3b^2}{2M^2}, \quad \alpha_{52} = \frac{4b}{M}. \quad (36)$$

The $1/r$ coefficients in Eq. (35) show that Kerr–Sen is outside the canonical asymptotically normalized Johannsen subclass unless an additional coordinate and mass parameter redefinition is performed. These examples should therefore be read as asymptotic coefficient identifications. A finite Johannsen truncation is a controlled phenomenological approximation to the large radius behavior of a target solution, not a global equality of the two metrics.

More generally, the Johannsen metric is not a solution of a specified set of field equations for arbitrary deviation functions. Its usefulness is instead phenomenological: with suitable choices of the deviation functions, it can be related to several known four dimensional black hole geometries discussed in alternative gravity or beyond-Kerr tests, including modified gravity bumpy Kerr metrics, slowly rotating dynamical Chern–Simons black holes, static Einstein–Dilaton–Gauss–Bonnet black holes, and rotating braneworld black holes [12, 51–54]. We use these mappings only as interpretive guidance for the deformation sectors, not as an assumption that the truncated metric solves any particular modified field equation.

The usual PPN restrictions can now be imposed as an additional weak field requirement. They are not used to derive the KG condition above; instead, they select the weak field normalization of the already separable metric. In the standard PPN framework [55–57], the spherically symmetric weak field reference metric may be written as

$$ds_{\text{PPN}}^2 = -A_{\text{PPN}}(r)dt^2 + B_{\text{PPN}}(r)dr^2 + r^2d\Omega^2, \quad (37)$$

with

$$\begin{aligned} A_{\text{PPN}}(r) &= 1 - \frac{2M}{r} + 2(\beta_{\text{PPN}} - \gamma_{\text{PPN}})\frac{M^2}{r^2}, \\ B_{\text{PPN}}(r) &= 1 + 2\gamma_{\text{PPN}}\frac{M}{r}. \end{aligned} \quad (38)$$

General relativity corresponds to $\beta_{\text{PPN}} = \gamma_{\text{PPN}} = 1$. Since KG separability has already fixed $g(\theta) = 0$, the large- r expansion of the asymptotically flat KG-separable Johannsen metric gives

$$ds^2 = -\left[1 - \frac{2M}{r} - \frac{M^2(2\alpha_{12} - \epsilon_2)}{r^2} + O(r^{-3})\right]dt^2 + \left[1 + \frac{2M}{r} + O(r^{-2})\right]dr^2 + r^2d\Omega^2. \quad (39)$$

Comparison with Eq. (37) yields

$$\begin{aligned} 2(\beta_{\text{PPN}} - \gamma_{\text{PPN}}) &= \epsilon_2 - 2\alpha_{12}, \\ \gamma_{\text{PPN}} &= 1, \end{aligned} \quad (40)$$

or equivalently

$$\beta_{\text{PPN}} - 1 = \frac{1}{2}(\epsilon_2 - 2\alpha_{12}). \quad (41)$$

Solar-System tests constrain this quantity to be very small [56, 57], which we denote schematically as

$$|\beta_{\text{PPN}} - 1| \ll 1. \quad (42)$$

Without a tuned cancellation between the two weak field coefficients, the PPN-compatible choice is

$$\epsilon_2 = \alpha_{12} = 0. \quad (43)$$

Combining Eq. (43) with Eq. (30) gives $\alpha_{22} = 0$. The PPN-compatible truncation used below is therefore not the most general KG-separable Johannsen subclass; it is the minimal weak field normalized representative used for the finite-frequency calculations. The working geometry used in the rest of this paper is therefore Eqs. (17)–(20) with $g(\theta) = 0$ and

$$\tilde{\Sigma} = r^2 + a^2 \cos^2 \theta + f(r), \quad (44)$$

and

$$A_1(r) = 1 + \alpha_{13} \left(\frac{M}{r}\right)^3 + \dots, \quad A_2(r) = 1 + \alpha_{23} \left(\frac{M}{r}\right)^3 + \dots, \quad (45)$$

$$A_5(r) = 1 + \alpha_{52} \left(\frac{M}{r}\right)^2 + \dots, \quad f(r) = \frac{(r^2 + a^2)A_1(r)}{A_2(r)} - (r^2 + a^2). \quad (46)$$

The same exterior regularity requirements used in the Johannsen parametrization constrain the leading coefficients. Requiring regularity outside the event horizon, absence of determinant singularities, preservation of the Lorentzian signature, and no closed timelike curves gives [12]

$$\begin{aligned} \alpha_{52} &> -\frac{(M + \sqrt{M^2 - a^2})^2}{M^2}, \\ \epsilon_3 &> -\frac{(M + \sqrt{M^2 - a^2})^3}{M^3}, \\ \alpha_{13} &> -\frac{(M + \sqrt{M^2 - a^2})^3}{M^3}, \\ \alpha_{22} &> -\frac{(M + \sqrt{M^2 - a^2})^2}{M^2}. \end{aligned} \quad (47)$$

For the weak field normalized KG-separable subclass, this bound is read together with $\alpha_{22} = 0$ and $\epsilon_3 = \alpha_{13} - \alpha_{23}$. Since the working parametrization uses α_{23} rather than the standard leading α_{22} as an independent input, the analytic bounds in Eq. (47) are supplemented in the numerical analysis by an explicit exterior-domain check of $\mathcal{D}(r, \theta)$, $\tilde{\Sigma}$, $A_5(r)$, and $g_{\phi\phi}$ for every parameter set used below. All parameter choices used in the following calculations and discussion are therefore taken inside this exterior regularity domain, within the KG-separable Johannsen subclass after imposing the PPN weak field normalization above.

III Scalar Wave Separation and Absorption Formalism

We now turn from the metric construction to the plane-wave absorption problem. In Sec. II the scalar mass μ was retained only to state the KG separability condition at the metric level. All numerical absorption calculations below set $\mu = 0$, so the asymptotic states are massless

scalar plane waves and can be compared directly with Kerr results. The governing equation is

$$\square\Phi = \frac{1}{\sqrt{-g}} \frac{\partial}{\partial x^\alpha} \left(\sqrt{-g} g^{\alpha\beta} \frac{\partial\Phi}{\partial x^\beta} \right) = 0. \quad (48)$$

We solve the radial scattering boundary-value problem in order to extract the transmission factors and absorption cross sections. Differential scattering cross sections are not considered in this work. Equation (25), together with the separability condition in Eq. (28), is then continued with the monochromatic mode decomposition

$$\Phi(t, r, \theta, \phi) = e^{-i\omega t} e^{im\phi} R_{lm}(r) S_{lm}(\theta). \quad (49)$$

Here ω is the real frequency measured with respect to the asymptotic time coordinate and m is the azimuthal number associated with the axial Killing field. For each fixed (ω, m) the integer $l \geq |m|$ labels the regular angular eigenfunction that enters the partial wave expansion of an incident plane wave. It is useful to introduce the radial size function

$$X(r) \equiv r^2 + a^2 + f(r) = \frac{(r^2 + a^2)A_1(r)}{A_2(r)} \quad (50)$$

and the radial wave factor

$$W(r) = A_2(r) [\omega X(r) - am]. \quad (51)$$

The symbol $X(r)$ is only a background function and should not be confused with the radial wave amplitude $R_{lm}(r)$.

Substitution of Eq. (49) separates the angular part into the same scalar spheroidal harmonic eigenvalue problem that appears in the Kerr scalar wave problem [24, 27, 58],

$$\frac{1}{\sin\theta} \frac{d}{d\theta} \left(\sin\theta \frac{dS_{lm}}{d\theta} \right) + \left[a^2\omega^2 \cos^2\theta - \frac{m^2}{\sin^2\theta} + \lambda_{lm}(a\omega) \right] S_{lm} = 0. \quad (52)$$

The eigenvalue $\lambda_{lm}(a\omega)$ reduces to $l(l+1)$ in the spherical limit $a\omega \rightarrow 0$. Since the angular equation is unchanged from Kerr, the standard scalar spheroidal basis and its selection rules can be used without modification. All Johannsen information relevant for the absorption amplitudes is therefore carried by the radial equation. With the same eigenvalue convention, the radial equation is

$$A_2\sqrt{A_5} \frac{d}{dr} \left(\frac{\Delta\sqrt{A_5}}{A_2} \frac{dR_{lm}}{dr} \right) + \left[\frac{W(r)^2}{\Delta} - \lambda_{lm}(a\omega) - a^2\omega^2 + 2am\omega \right] R_{lm} = 0, \quad (53)$$

Equivalently, after defining

$$\Lambda_{lm} \equiv \lambda_{lm}(a\omega) + a^2\omega^2 - 2am\omega, \quad (54)$$

it can be written as

$$A_2\sqrt{A_5} \frac{d}{dr} \left(\frac{\Delta\sqrt{A_5}}{A_2} \frac{dR_{lm}}{dr} \right) + \left[\frac{W(r)^2}{\Delta} - \Lambda_{lm} \right] R_{lm} = 0. \quad (55)$$

The Kerr limit is recovered by setting $A_1 = A_2 = A_5 = 1$ and $f = 0$, for which $X = r^2 + a^2$ and

$$W = \omega(r^2 + a^2) - am.$$

The structure of Eq. (55) makes the role of the three leading deformation sectors transparent. The functions A_1 and A_2 determine $X(r)$ through Eq. (50), so they change the algebraic wave factor $W(r)$, the horizon angular velocity, and the turning point structure of the high-frequency problem. By contrast, A_5 enters only through the radial kinetic operator and the tortoise map. It therefore leaves the angular equation and, for a pure A_5 deformation, the geometric capture boundary unchanged, while still modifying the finite-frequency radial propagation.

To put the radial equation into a Schrödinger-like wave form we define

$$\frac{dr_*}{dr} = \frac{A_2(r)X(r)}{\Delta(r)\sqrt{A_5(r)}}, \quad U_{lm}(r) = \sqrt{X(r)} R_{lm}(r), \quad (56)$$

and

$$\Xi(r) \equiv \frac{dr}{dr_*} = \frac{\Delta(r)\sqrt{A_5(r)}}{A_2(r)X(r)}. \quad (57)$$

The radial equation becomes

$$\frac{d^2 U_{lm}}{dr_*^2} + \left[\left(\omega - \frac{ma}{X(r)} \right)^2 - V_{lm}^J(r) \right] U_{lm} = 0, \quad (58)$$

where the Johannsen scalar wave potential is

$$V_{lm}^J(r) = \frac{\Delta \Lambda_{lm}}{A_2(r)^2 X(r)^2} + \frac{\Xi(r)}{2X(r)} \frac{d}{dr} \left(\Xi(r) \frac{dX}{dr} \right) - \frac{\Xi(r)^2}{4} \left(\frac{1}{X(r)} \frac{dX}{dr} \right)^2. \quad (59)$$

This form keeps the frame dragging frequency $\omega - ma/X(r)$ outside the potential. The potential itself vanishes at both the event horizon and spatial infinity under the asymptotic flatness and regularity assumptions used here. Thus the two ends of the exterior region are asymptotic wave regions, while the finite radial domain between them acts as the effective barrier, as in the standard black hole absorption construction [27].

The potential plot in Fig. 1 gives a direct radial view of Eq. (59). The deformation does not merely rescale the Kerr barrier. In the representative $(l, m) = (1, 1)$ mode, the A_1 sector gives the largest change near the inner side of the barrier, while the A_2 and A_5 sectors produce smaller but distinct radial responses. All deviations decay rapidly at large radius, as required by asymptotic flatness. The A_5 curve nearly overlaps with Kerr in the upper panel, but the lower panel resolves a nonzero residual. Thus, even though A_5 drops out of the angular equation and of the leading null capture boundary, it still changes the finite-frequency radial propagation through the kinetic operator and the tortoise map. For comparison with the actual radial wave coordinate, Appendix A also displays the same potential curves as functions of the tortoise coordinate in Fig. 8; the near horizon stretching changes the horizontal shape of the barrier but not the sector dependent conclusion drawn here.

Let

$$r_+ = M + \sqrt{M^2 - a^2}, \quad \Omega_H = \frac{a}{X(r_+)}, \quad \tilde{\omega}_m \equiv \omega - m\Omega_H. \quad (60)$$

The shifted frequency $\tilde{\omega}_m = \omega - m\Omega_H$ is the Killing frequency associated with the horizon-generating vector $\chi = \partial_t + \Omega_H \partial_\phi$, or equivalently the mode frequency in the frame co-rotating

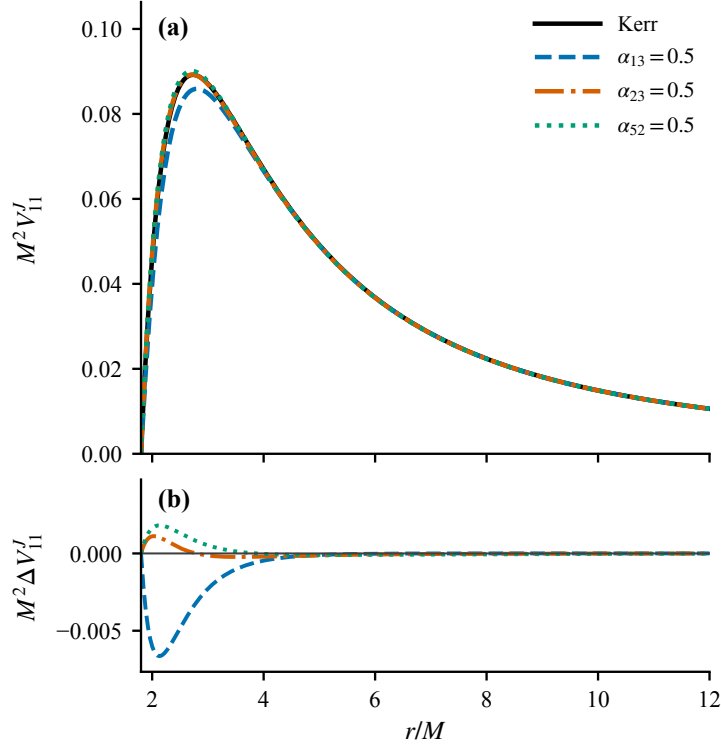


Figure 1: Dimensionless scalar wave effective potential $M^2 V_{l1}^J$ for representative leading Johannsen deformations. The upper panel compares Kerr with the single parameter cases $\alpha_{13} = 0.5$, $\alpha_{23} = 0.5$, and $\alpha_{52} = 0.5$ at $a/M = 0.6$ and $M\omega = 0.3$. The lower panel shows the corresponding difference relative to Kerr, making the sector dependent radial response visible. This potential is not a coordinate invariant observable; it is used only as a diagnostic of the radial wave barrier in the scattering form of Eq. (58).

with the horizon. The physical “in” solution is chosen to be purely ingoing at the future horizon and to contain incident plus reflected waves at spatial infinity:

$$U_{lm} \sim \begin{cases} A_{\text{in}} U_{\omega lm}^{\infty, \text{in}} + A_{\text{out}} U_{\omega lm}^{\infty, \text{out}}, & r_* \rightarrow +\infty, \\ T_{\omega lm} U_{\omega lm}^{H, \text{in}}, & r_* \rightarrow -\infty. \end{cases} \quad (61)$$

This is the usual flux normalization for black hole absorption: A_{in} , A_{out} , and $T_{\omega lm}$ are the incident, reflected, and transmitted amplitudes, respectively. For numerical matching, one then represents the local ingoing bases by asymptotic series, as in the standard Kerr and Kerr-Newman treatments [27, 38],

$$U_{\omega lm}^{\infty, \text{in}}(r) = e^{-i\omega r_*} \sum_{j=0}^{N_{\infty}} \frac{c_j^{\infty}}{r^j}, \quad r_* \rightarrow +\infty, \quad (62)$$

$$U_{\omega lm}^{H, \text{in}}(r) = e^{-i\hat{\omega} r_*} \sum_{j=0}^{N_+} c_j^+ (r - r_+)^j, \quad r_* \rightarrow -\infty. \quad (63)$$

The coefficients c_j^{∞} and c_j^+ are obtained by requiring $U_{\omega lm}^{\infty, \text{in}}$ and $U_{\omega lm}^{H, \text{in}}$ to solve the radial equation order by order in the two asymptotic regions. Their overall normalization is a matching convention

and is absorbed into the wave amplitudes. The outgoing basis at infinity is $U_{\omega lm}^{\infty, \text{out}} \equiv (U_{\omega lm}^{\infty, \text{in}})^*$ for real ω .

Conservation of the radial Wronskian gives

$$\left| \frac{A_{\text{out}}}{A_{\text{in}}} \right|^2 = 1 - \frac{\tilde{\omega}_m}{\omega} \left| \frac{T_{\omega lm}}{A_{\text{in}}} \right|^2. \quad (64)$$

Therefore modes satisfying $\tilde{\omega}_m < 0$, or $0 < \omega < m\Omega_H$ for $m\Omega_H > 0$, are superradiantly amplified: the reflected flux exceeds the incident flux. This is the usual rotating black hole superradiance mechanism [25, 26]. In the present notation it appears as a negative signed absorption factor rather than as a failure of the flux normalization.

The signed absorption factor is defined from the reflection amplitude as

$$\Gamma_{\omega lm} = 1 - \left| \frac{A_{\text{out}}}{A_{\text{in}}} \right|^2 = \frac{\tilde{\omega}_m}{\omega} \left| \frac{T_{\omega lm}}{A_{\text{in}}} \right|^2, \quad (65)$$

In the superradiant regime $0 < \omega < m\Omega_H$, this quantity is a signed absorption factor: $\Gamma_{\omega lm} < 0$ corresponds to superradiant amplification rather than to a positive transmission probability. We therefore also use the amplification factor

$$Z_{\text{amp}} = \left| \frac{A_{\text{out}}}{A_{\text{in}}} \right|^2 - 1 = -\Gamma_{\omega lm}$$

when discussing superradiance. This completes the radial boundary data needed for the absorption problem.

IV Absorption Cross Section and Limiting Regimes

The observable absorption cross section is assembled from the radial signed absorption factors and the scalar spheroidal harmonics. With the standard plane wave normalization, the partial absorption cross section for an incidence angle γ is

$$\sigma_{lm}(\omega, \gamma) = \frac{4\pi^2}{\omega^2} |S_{\omega lm}(\gamma)|^2 \Gamma_{\omega lm}. \quad (66)$$

The total finite-frequency absorption cross section is then obtained from the partial wave sum

$$\sigma_{\text{abs}}(\omega, \gamma) = \sum_{l=0}^{\infty} \sum_{m=-l}^l \sigma_{lm}(\omega, \gamma). \quad (67)$$

For off-axis incidence it is useful to split the mode sum into co-/counter-rotating azimuthal sectors,

$$\sigma_+(\omega, \gamma) = \sum_{l=0}^{\infty} \sum_{m=1}^l \sigma_{lm}(\omega, \gamma) + \frac{1}{2} \sum_{l=0}^{\infty} \sigma_{l0}(\omega, \gamma), \quad (68)$$

$$\sigma_-(\omega, \gamma) = \sum_{l=0}^{\infty} \sum_{m=-l}^{-1} \sigma_{lm}(\omega, \gamma) + \frac{1}{2} \sum_{l=0}^{\infty} \sigma_{l0}(\omega, \gamma), \quad (69)$$

so that $\sigma_{\text{abs}} = \sigma_+ + \sigma_-$. This is a bookkeeping convention rather than a new observable; the $m = 0$ sector is divided equally because it carries no azimuthal preference. For a black hole with $a > 0$, the $m > 0$ modes are the co-rotating sector in this convention, while $m < 0$ modes are counter-rotating. The physical distinction enters through the radial factor $\omega - ma/X(r)$ and the horizon frequency $\tilde{\omega}_m = \omega - m\Omega_H$. Co-rotating modes can be closer to the superradiant window and are therefore more strongly affected by rotational energy exchange, whereas counter-rotating modes are never superradiant for $\omega > 0$ and $a > 0$. The asymmetry between σ_+ and σ_- is thus a direct finite-frequency probe of frame dragging and of the deformation dependence of $X(r)$ and Ω_H .

In numerical work the sums are truncated at L_{max} and increased until the tail is negligible. For on-axis incidence only the $m = 0$ modes contribute, whereas equatorial incidence imposes the usual parity selection on the scalar spheroidal functions. These selection rules are inherited directly from the Kerr angular problem; all Johannsen dependence enters through the radial signed absorption factors.

A Low-Frequency Limit

In the zero-frequency limit the scalar absorption cross section approaches the horizon area,

$$\sigma_{\text{abs}}(\omega \rightarrow 0) \rightarrow A_H. \quad (70)$$

This is the standard area law for a minimally coupled massless scalar in stationary black hole backgrounds under the usual regularity assumptions on the zero-frequency solution [32–34]. For the working Johannsen subclass the induced metric on a spatial horizon section gives

$$A_H = \int_0^{2\pi} d\phi \int_0^\pi d\theta \sqrt{g_{\theta\theta}g_{\phi\phi}} \Big|_{r=r_+} = 4\pi X(r_+) = 4\pi \frac{(r_+^2 + a^2)A_1(r_+)}{A_2(r_+)}. \quad (71)$$

The last equality uses the KG separability condition $(r^2 + a^2)A_1 = XA_2$. Equation (71) makes the sector dependence transparent: A_1 increases or decreases the area through the numerator, A_2 changes it inversely, and A_5 has no direct effect because it only appears in the radial metric component. The low-frequency rows of Table 1 reflect precisely this structure. For the positive leading coefficients shown there, $\alpha_{13} = 0.5$ increases A_H , $\alpha_{23} = 0.5$ decreases it, and $\alpha_{52} = 0.5$ leaves the Kerr area unchanged at every spin.

B High-Frequency Limit

In the high-frequency limit, the wave problem reduces to the capture of null geodesics. For an incidence angle γ , the geometric cross section is the area of the critical capture region on the incident wavefront. Following the impact plane construction used for Kerr [28], this area can be written as

$$\sigma_{\text{geo}}(\gamma) = \frac{1}{2} \int_{-\pi}^{\pi} b_c^2(\chi, \gamma) d\chi, \quad (72)$$

where χ is the polar angle on the wavefront and $b_c(\chi, \gamma)$ is the critical impact parameter separating captured and scattered rays. For each direction on the wavefront it is determined by the unstable

circular orbit conditions

$$\mathcal{R}_{\text{geo}}(r_c) = 0, \quad \frac{d\mathcal{R}_{\text{geo}}}{dr}(r_c) = 0. \quad (73)$$

Here \mathcal{R}_{geo} denotes the radial Hamilton–Jacobi potential for null geodesics. The crucial Johannsen feature is that A_5 multiplies the radial kinetic term but does not enter the algebraic conditions (73). Hence A_5 can modify finite-frequency radial propagation without moving the geometric capture boundary.

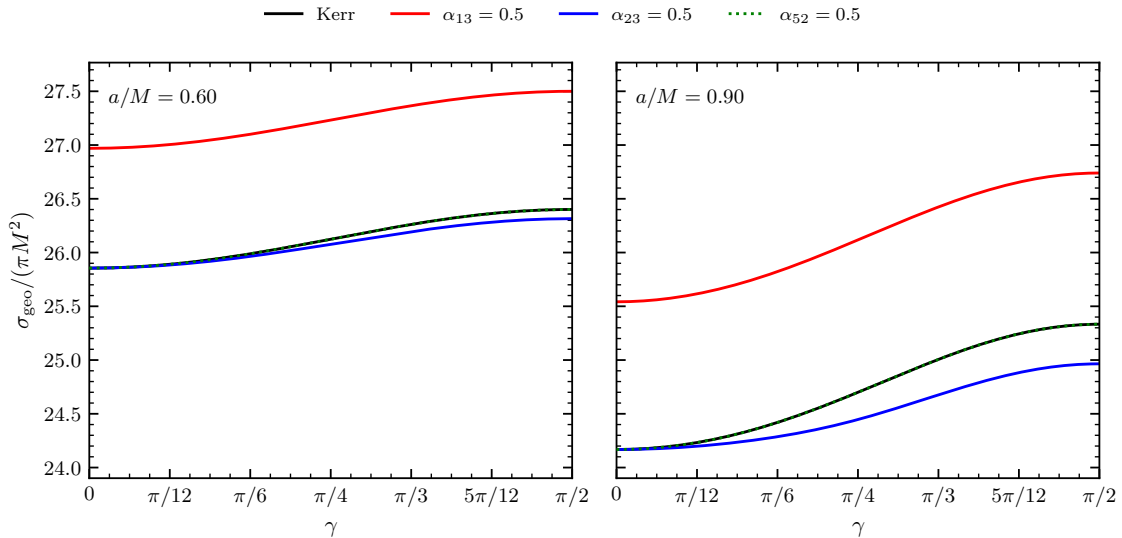


Figure 2: High-frequency geometric capture cross section as a function of incidence angle for $a/M = 0.6$ and $a/M = 0.9$. The A_5 deformation is degenerate with Kerr in geometric optics, while A_1 and A_2 change the null capture boundary.

The incidence-angle scan in Fig. 2 makes this separation of sectors explicit. Comparing the two spin values also makes the spin dependence visible: increasing the Kerr spin parameter from $a/M = 0.6$ to $a/M = 0.9$ lowers the overall capture area for the displayed families. This decrease reflects the shrinkage and distortion of the critical null capture region at higher rotation, rather than a uniform rescaling of the impact plane. The A_1 sector changes the effective radial size $X(r)$ and therefore shifts the capture area already for on-axis incidence. The A_2 sector is more selective: it can be degenerate with Kerr in the on-axis entries of Table 1, but its deviation grows with incidence angle, and the departure is more pronounced at $a/M = 0.9$ than at $a/M = 0.6$. This reflects the fact that the A_2 deformation enters the spin-coupled azimuthal part of the null capture conditions. By contrast, the A_5 curve lies on top of Kerr for both displayed spins, confirming its invisibility to the leading null capture observable. This does not mean that A_5 is absent from the spacetime geometry; it remains part of the radial metric component. The equality is also visible in Table 1: the on-axis high-frequency entries for $\alpha_{52} = 0.5$ are identical to Kerr for all listed spins.

The approach to σ_{geo} is not monotonic. Schwarzschild calculations by Sanchez showed that the high-frequency absorption cross section oscillates around the geometric limit [23]. Complex angular momentum analyses later related this oscillatory pattern to Regge poles and to the orbital frequency and Lyapunov exponent of unstable null geodesics [36, 37]. For a static spherically symmetric black hole with critical impact parameter b_c , orbital frequency Ω , Lyapunov exponent

Λ , and $\beta = \Lambda/\Omega$, the leading sinc approximation can be written as

$$\frac{\sigma_{\text{abs}}(\omega)}{\sigma_{\text{geo}}} \simeq 1 - 8\pi\beta e^{-\pi\beta} \text{sinc}\left(\frac{2\pi\omega}{\Omega}\right), \quad \text{sinc } x \equiv \frac{\sin x}{x}. \quad (74)$$

For Schwarzschild, $\Omega = 1/b_c$ and $\beta = 1$. For on-axis incidence on a rotating black hole, the same physical idea survives but the polar photon orbit has $b_c \neq 1/\Omega$. Motivated by the Kerr on-axis approximation of Macedo et al. [28], we use the following Johannsen polar-orbit analogue as a qualitative high-frequency guide:

$$\frac{\sigma_{\text{abs}}(\omega)}{\sigma_{\text{geo}}} \simeq 1 - \frac{8\pi\beta e^{-\pi\beta}}{\Omega^2 b_c^2} \text{sinc}\left(\frac{2\pi\omega}{\Omega}\right), \quad \beta = \frac{\Lambda}{\Omega}, \quad (75)$$

where b_c , Ω , and Λ are computed from the unstable polar null orbit of the Johannsen geometry. In the present work this approximation is used as a high-frequency guide rather than as a replacement for the finite-frequency mode sum. It clarifies which part of the oscillatory absorption spectrum is controlled by null orbit data and which part must still be attributed to the full radial wave propagation. The dotted curves shown with the on-axis spectra below are generated from Eq. (75).

Table 1: Low- and high-frequency limits of the scalar absorption cross section. The low-frequency limit is the horizon area, while the high-frequency limit is the on-axis geometric capture cross section. All values are given in units of πM^2 .

Model	Limit	$a/M = 0$	$a/M = 0.3$	$a/M = 0.6$	$a/M = 0.9$	$a/M = 0.99$
Kerr	$\sigma(\omega \simeq 0)$	16.000	15.632	14.400	11.487	9.129
	$\sigma(\omega M \gg 1)$	27.000	26.726	25.855	24.168	23.409
$\alpha_{13} = 0.5$	$\sigma(\omega \simeq 0)$	17.000	16.679	15.635	13.427	12.201
	$\sigma(\omega M \gg 1)$	27.982	27.738	26.969	25.542	24.937
$\alpha_{23} = 0.5$	$\sigma(\omega \simeq 0)$	15.059	14.650	13.263	9.827	6.830
	$\sigma(\omega M \gg 1)$	27.000	26.726	25.855	24.168	23.409
$\alpha_{52} = 0.5$	$\sigma(\omega \simeq 0)$	16.000	15.632	14.400	11.487	9.129
	$\sigma(\omega M \gg 1)$	27.000	26.726	25.855	24.168	23.409

V Finite-Frequency Absorption Results

The numerical calculation follows the partial wave construction in Sec. IV. For each (ω, l, m) we first compute the scalar spheroidal eigenvalue, then integrate the Johannsen radial equation from the near horizon region to the asymptotic matching region, and finally assemble the cross section from the signed absorption factors. For each relative deviation and root-mean-square (RMS) diagnostic, the Kerr reference spectrum is recomputed on the same frequency grid rather than interpolated from a separate dataset. The radial integration starts from the ingoing horizon expansion and is matched to independent ingoing and outgoing asymptotic solutions at large radius. The initial-value problem is solved in the Boyer–Lindquist-like radius using an adaptive high-order Runge–Kutta method (DOP853), with production tolerances typically set to $\text{rtol} = 10^{-9}$ and $\text{atol} = 10^{-11}$ and tightened in targeted reruns when matching diagnostics require it. Expansion orders and matching radii are raised until the extracted absorption factor

is stable. On-axis spectra use the exact $m = 0$ selection rule, whereas off-axis spectra use the full triangular mode set $0 \leq l \leq L_{\max}$ and $-l \leq m \leq l$. In all production plots the mode cutoff is increased until the pointwise cross section sum is trusted, with targeted radial reruns used only for isolated points that fail the matching or truncation checks.

Before discussing the spectra, we quantify why the leading Johannsen coefficients are used as the main deformation parameters. For one active coefficient of radial falloff order n , define the pointwise relative deviation and its RMS average over a fixed frequency grid by

$$\delta_n(\omega_j) = \frac{\sigma_n(\omega_j) - \sigma_{\text{Kerr}}(\omega_j)}{\sigma_{\text{Kerr}}(\omega_j)}, \quad (76)$$

$$S_n = \left[\frac{1}{N_\omega} \sum_{j=1}^{N_\omega} \delta_n(\omega_j)^2 \right]^{1/2}. \quad (77)$$

Only points for which both the Johannsen numerator and the Kerr denominator pass the trust checks enter S_n .

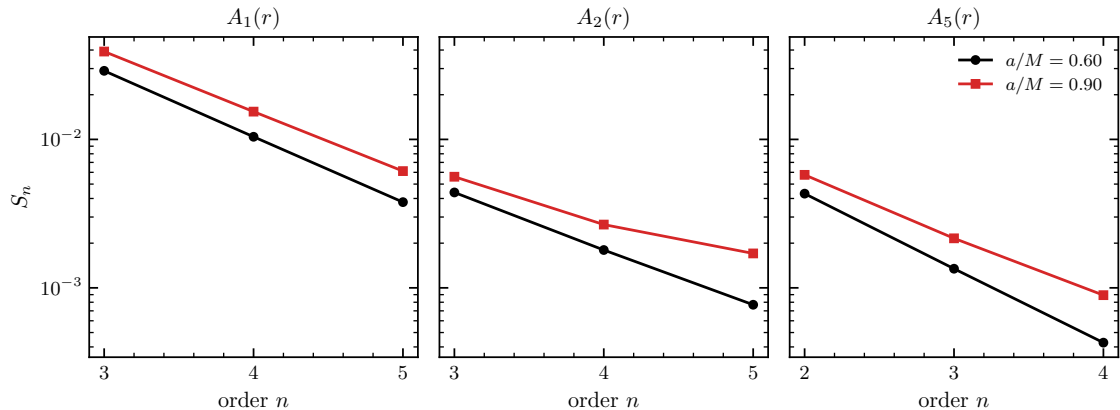


Figure 3: Hierarchy of Johannsen coefficients with increasing radial falloff. The plotted quantity is the RMS sensitivity S_n defined by Eqs. (76) and (77), with $M = 1$, $\gamma = 0$, coefficient amplitude $p = 0.3$, $\omega M \in [0.1, 1.5]$, and $N_\omega = 101$. The Kerr denominators are recomputed on the same grid for each spin. The panels correspond to the A_1 , A_2 , and A_5 sectors.

The trend extracted in Fig. 3 is monotonic in all sampled sectors: the absorption response decreases as the radial falloff order is raised. This does not prove that every possible higher order deformation is negligible, but it supports a controlled leading coefficient study: for the same asymptotic coefficient amplitude, the lowest allowed powers give the largest finite-frequency response. The frequency resolved curves underlying this RMS compression are given in Appendix A.

The validation strategy is tied to the limiting results of Sec. IV. The same code recovers the Kerr limit, checks $\sigma = \sigma^+ + \sigma^-$ whenever a co-/counter-rotating split is computed, verifies the low-frequency approach to the horizon area, and compares the high-frequency envelope with the geometric capture values in Table 1. These tests are important because the finite-frequency differences discussed below are typically smaller than the gross variation of the total cross section with spin.

A Leading-Order On-Axis Spectra

We first consider on-axis incidence, $\gamma = 0$, for which only the $m = 0$ spheroidal harmonics contribute to the incident plane wave. This setup is a clean baseline because it removes the azimuthal mixing associated with off-axis incidence while retaining the full radial boundary-value problem. The spectra in Fig. 4 compare Kerr with the three single parameter Johannsen families $\alpha_{13} = 0.5$, $\alpha_{23} = 0.5$, and $\alpha_{52} = 0.5$.

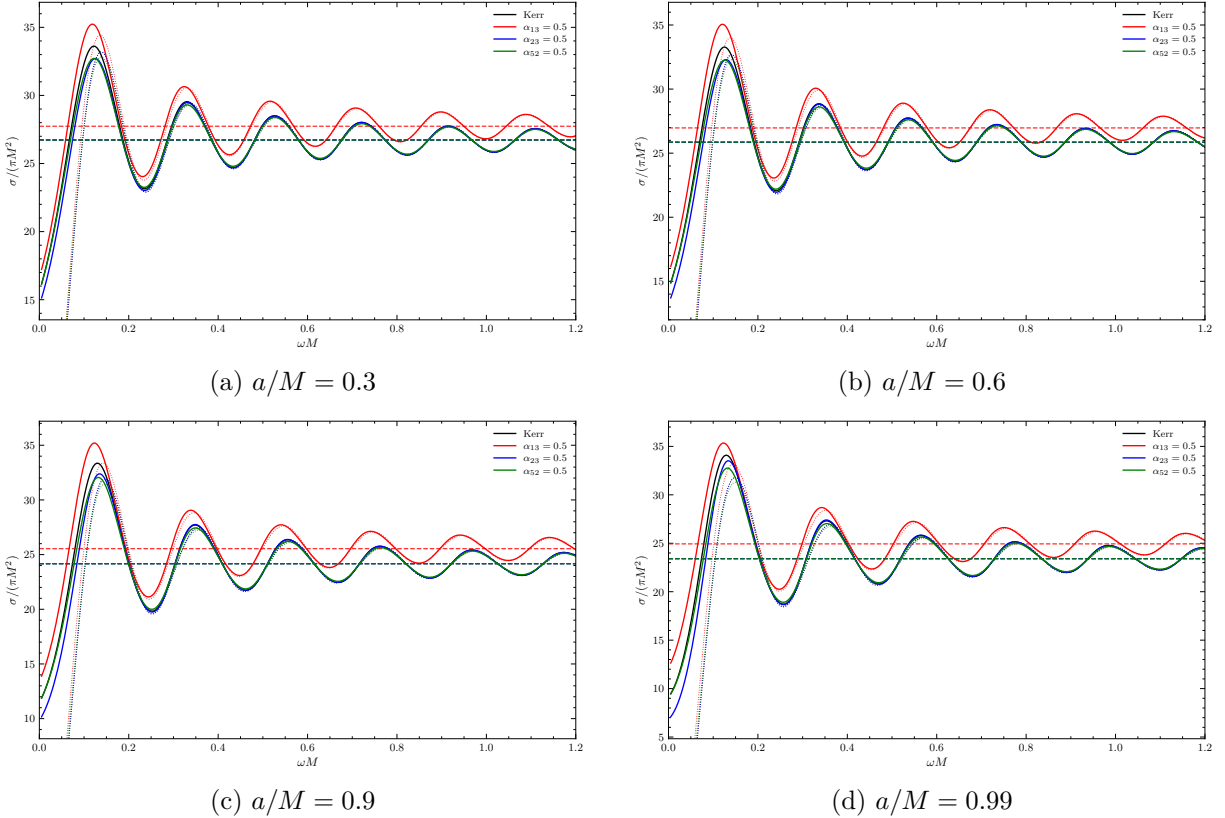


Figure 4: On-axis total absorption spectra for Kerr and for the leading Johannsen deformations with coefficient amplitude 0.5. The dashed horizontal lines show the corresponding high-frequency geometric capture limits, and the dotted curves show the associated high-frequency sinc estimates from Eq. (75).

The low-frequency ordering follows the area formula in Eq. (71): positive α_{13} increases A_H , positive α_{23} decreases it through the denominator $A_2(r_+)$, and positive α_{52} leaves it unchanged. The same pattern is visible in the first rows of Table 1 and in the left edge of the spectra. In the high-frequency regime the curves approach the geometric reference lines discussed in Sec. IV.B. The A_5 curves again share the Kerr limiting value, while the finite-frequency part of the spectrum is shifted because A_5 enters the radial kinetic operator and the tortoise coordinate. This is the first numerical indication that finite-frequency absorption probes more structure than the two limiting cross sections.

To isolate the sector dependence, we use the relative deviation

$$\frac{\delta\sigma}{\sigma_{\text{Kerr}}} = \frac{\sigma_{\text{J}} - \sigma_{\text{Kerr}}}{\sigma_{\text{Kerr}}}. \quad (78)$$

This normalization removes the common Kerr envelope and makes the sign, frequency location, and oscillatory phase of each deformation easier to compare.

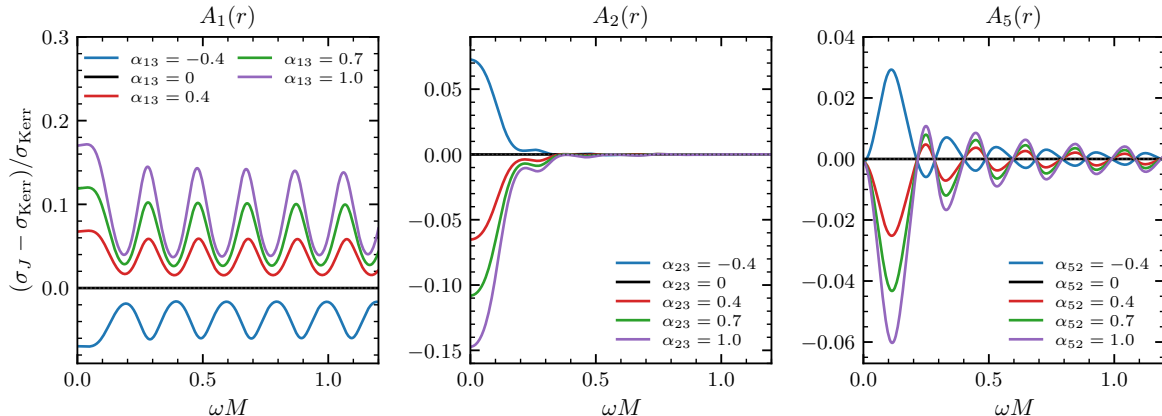


Figure 5: Relative deviations from Kerr by deformation sector for on-axis incidence at fixed spin $a/M = 0.6$ and $\gamma = 0$. From left to right the panels show the A_1 , A_2 , and A_5 sectors; in each panel only the corresponding leading Johannsen parameter is varied.

The relative spectra in Fig. 5 make clear that the three metric sectors do not act as interchangeable rescalings of the Kerr spectrum. The deviations are not merely smooth offsets: the A_1 and A_5 sectors in particular show oscillatory structure across the finite-frequency range. This behavior reflects changes in the radial barrier and in the relative phase of the partial-wave absorption pattern, and the same frequency-resolved behavior is visible in the hierarchy curves shown in Fig. 9. The A_1 and A_2 panels carry the expected imprint of the low- and high-frequency limits, because these functions enter $X(r)$ and hence both A_H and the geometric capture problem. The A_5 sector is qualitatively different. Its geometric cross section coincides with Kerr for the full incidence-angle range shown in Fig. 2, yet its finite-frequency relative deviation is nonzero. The comparison should not be read as a point-by-point comparison between an on-axis wave spectrum and an off-axis geometric scan. Rather, it identifies the mechanism: A_5 is absent from the leading null capture boundary but present in the radial wave propagation. It is therefore geometry-invisible only in the restricted sense of the leading null capture observable, but wave-visible at finite frequency. The corresponding total absorption curves are shown in Appendix A.

B Angular Dependence and Azimuthal Asymmetry

Off-axis incidence activates the full set of azimuthal modes and tests whether the conclusions above are artifacts of the on-axis $m = 0$ selection rule. We use the co-/counter-rotating split in Eqs. (68) and (69) to define

$$\mathcal{A}(\omega) = \frac{\sigma^-(\omega) - \sigma^+(\omega)}{\sigma^-(\omega) + \sigma^+(\omega)}. \quad (79)$$

For the sign convention used here, $\mathcal{A} > 0$ means that the counter-rotating sector contributes more strongly to the absorption sum, whereas $\mathcal{A} < 0$ means that the co-rotating sector dominates.

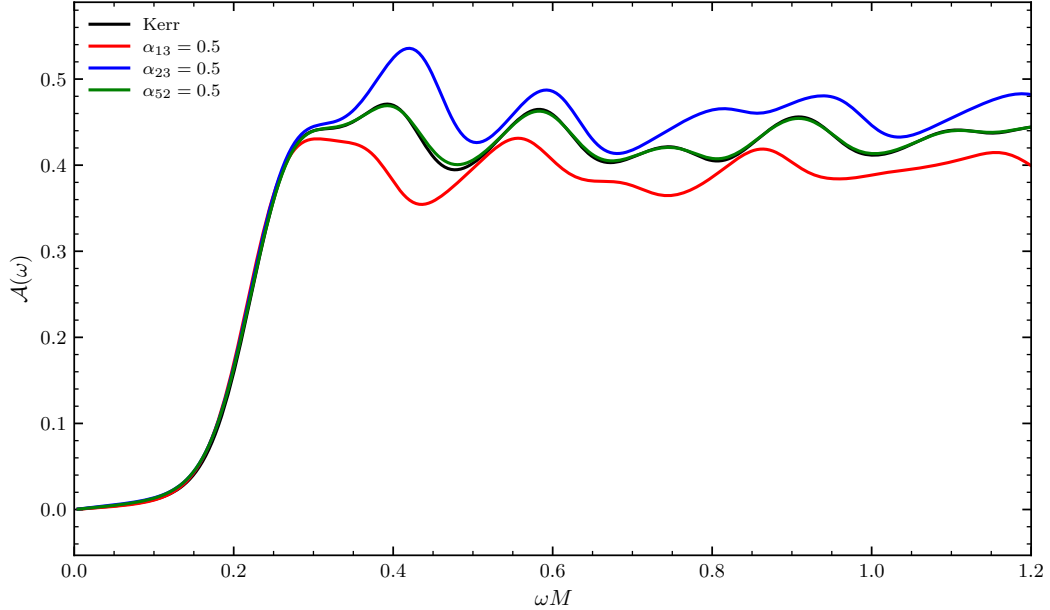


Figure 6: Azimuthal asymmetry for off-axis incidence at $a/M = 0.9$ and $\gamma = \pi/3$, measured by $\mathcal{A}(\omega)$ in Eq. (79). The calculation uses the full triangular mode set rather than the on-axis $m = 0$ selection rule.

In Fig. 6, the off-axis calculation produces a clear frequency dependent imbalance between the two azimuthal sectors. This imbalance is expected for rotating holes: positive and negative m modes experience different frame dragging shifts in $\omega - ma/X(r)$ and different horizon frequencies $\tilde{\omega}_m$. Johannsen deformations modify this imbalance in a sector dependent way. A_1 and A_2 change $X(r)$ and Ω_H directly, while A_5 modifies the radial transmission problem without changing the geometric capture boundary. The A_5 curve is therefore close to Kerr but not identical, which is another finite-frequency imprint of the radial kinetic sector. The result confirms that the finite-frequency signal is not restricted to the on-axis special case. A direct plot of σ^+ and σ^- is included in Appendix A to show that Fig. 6 is not produced by a denominator artifact.

C Single-Mode Superradiance

The signed absorption factor in Eq. (65) also carries the superradiant information. In the usual rotating black hole window $0 < \omega < m\Omega_H$, the reflected flux is larger than the incident flux and $\Gamma_{\omega lm} < 0$ [25, 26]. Through Eq. (66), the corresponding single-mode contribution to the plane-wave absorption cross section becomes negative in this interval. We therefore plot the $l = m = 1$ partial absorption cross section at $a/M = 0.99$ and $\gamma = \pi/2$, using an inset to resolve the narrow negative band while keeping the finite-frequency scale of the mode visible in the main panel. An equivalent positive amplification factor,

$$Z_{\text{amp}}(\omega) = \left| \frac{A_{\text{out}}}{A_{\text{in}}} \right|^2 - 1 = -\Gamma_{\omega lm}, \quad 0 < \omega < m\Omega_H, \quad (80)$$

is displayed separately in Appendix A.

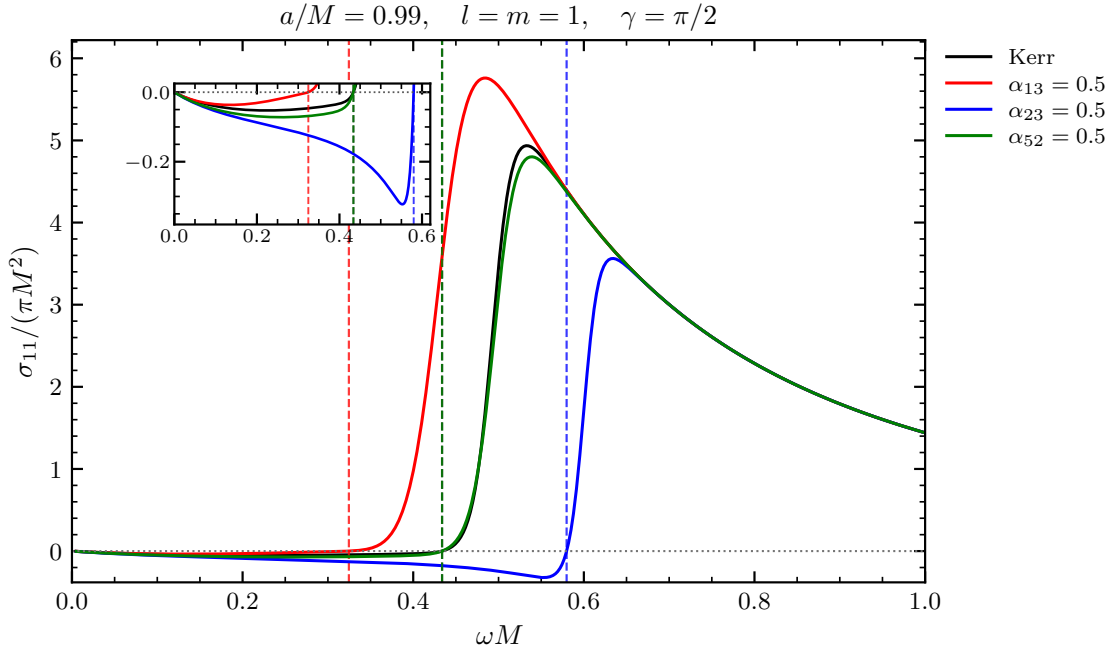


Figure 7: Partial absorption cross section $\sigma_{11}/(\pi M^2)$ for the $l = m = 1$ scalar mode at $a/M = 0.99$ and $\gamma = \pi/2$. The main panel shows the finite-frequency scale of this mode, while the inset magnifies the low-frequency superradiant regime, where $\Gamma_{\omega 11} < 0$ and hence $\sigma_{11} < 0$. Negative values in the inset are a mode-level superradiant effect and do not imply a negative total absorption cross section. The vertical dashed lines mark the thresholds $\omega = m\Omega_H$ for the corresponding cases.

Figure 7 should be read as a mode-resolved partial absorption plot rather than as a total cross section. The main panel shows that the same $l = m = 1$ contribution becomes positive and grows outside the superradiant band, whereas the inset isolates the negative low-frequency portion. The horizon angular velocity is $\Omega_H = a/X(r_+)$, so any deformation that changes $X(r_+)$ also changes the edge of the superradiant band. For the positive coefficients shown here, $\alpha_{13} = 0.5$ increases $X(r_+)$ and shifts the threshold to smaller ωM , whereas $\alpha_{23} = 0.5$ decreases $X(r_+)$ and pushes the threshold upward. A pure α_{52} deformation leaves $X(r_+)$, and therefore Ω_H , equal to the Kerr value, but it still affects the detailed radial transmission through the radial kinetic term. The superradiant mode therefore gives another example of the same sector separation found in the absorption spectra: the threshold is controlled by the horizon value of $X(r)$, while the shape and depth of the partial-cross-section curve are sensitive to the full wave operator.

VI Discussion and Conclusion

We have constructed the scalar absorption problem for a Klein–Gordon-separable Johannsen subclass and traced the leading deformation sectors through their analytic limits and the finite-frequency partial-wave calculation. The separability condition ties the Johannsen radial functions through $X(r) = (r^2 + a^2)A_1/A_2$, leaving three independent sectors in the simplified PPN compatible model: A_1 , A_2 , and A_5 . This structure is physically instructive because it cleanly separates metric components that govern the horizon area and null-capture geometry from those that modify only the radial wave propagation.

Our central result is that finite-frequency wave absorption resolves a fundamental degeneracy inherent to purely geometric probes. The functions A_1 and A_2 change the radial size function $X(r)$ and therefore appear in the low-frequency area law, in the high-frequency capture cross section, and in finite-frequency spectra. In contrast, A_5 changes the radial kinetic operator and the tortoise coordinate, but does not change the horizon area or the null geodesic capture boundary for a pure A_5 deformation. The finite-frequency relative deviation curves nevertheless show a nonzero response to α_{52} . This constitutes the primary novel finding of our calculation: the A_5 sector is invisible to both the low-frequency area law and the leading high-frequency null-capture observable, yet it becomes manifest once wave-optics effects are included at finite frequencies. In other words, scalar wave absorption provides a diagnostic of radial propagation sectors that remain entirely degenerate in geometric-optics observables.

This wave-mechanical discrimination carries direct significance for strong-field tests of the no-hair theorem. Because geometric probes such as shadow morphology and null-capture cross sections are insensitive to pure A_5 -type deformations, they cannot alone exhaust the space of possible Kerr deviations. Our results demonstrate that finite-frequency absorption cross sections can break this degeneracy, offering a complementary probe of metric deformations that geometric methods miss. Consequently, wave-optics observables—accessible through black hole absorption, quasinormal mode spectroscopy, and related scattering phenomena—are essential for a complete and systematic test of whether astrophysical black holes are uniquely described by the Kerr geometry, or whether they harbor deviations permitted by more general stationary, axisymmetric spacetimes.

This perspective is consistent with recent full-wave studies of regular black-hole backgrounds. In the Frolov case, the absorption and scattering spectra of Frolov, Reissner–Nordström, and Hayward geometries were found to become nearly indistinguishable once the relevant critical or glory impact parameters were matched, emphasizing the leading role of photon-sphere data in the intermediate-to-high-frequency regime [46]. The Johannsen calculation here addresses a complementary question: rather than matching different static geometries by their photon-sphere scales, we isolate a rotating deformation sector, A_5 , that is invisible to the leading null-capture observable but remains visible in the finite-frequency radial wave problem.

The numerical hierarchy test provides a consistency check on this interpretation: at fixed asymptotic coefficient amplitude, the lowest allowed powers produce the largest finite-frequency response, supporting the use of α_{13} , α_{23} , and α_{52} as the primary deformation parameters. Furthermore, the off-axis calculation, the co-/counter-rotating asymmetry, and the single-mode superradiant threshold all confirm that the sector-dependent signal is not an artifact of the on-axis $m = 0$ selection rule. In particular, A_1 and A_2 shift $X(r_+)$ and therefore the horizon angular velocity $\Omega_H = a/X(r_+)$, moving the superradiant threshold, whereas A_5 leaves the threshold location unchanged but still modifies the radial amplification profile—another manifestation of the same wave-visible/geometric-invisible separation.

Several qualifications should be kept explicit. The calculation is performed for a test, massless scalar field, so it does not include backreaction, massive field bound states, or spin-dependent couplings. The Johannsen functions are treated in a truncated leading-coefficient model; this is motivated by the hierarchy test, but it is not a proof that every higher-order combination is

observationally negligible. Finally, the mapping between finite Johannsen truncations and exact alternatives to Kerr should be interpreted as a weak-field or sector-level comparison rather than a unique global identification.

Our framework can be extended in several directions. The most direct next step is a broader parameter survey, including incidence-angle dependence, larger spin grids, and systematic comparisons with exact separable metrics such as Kerr–Newman or Kerr–Sen where available. A second direction is to move beyond massless scalar waves, either by including a field mass or by studying electromagnetic and gravitational perturbations. More broadly, the method developed here can be carried to more general rotating black holes, including parametrized or specific theoretical geometries whose separability properties differ from the Johannsen subclass. In that setting, absorption, shadows, quasinormal mode spectra, and superradiant amplification could be compared within a unified strong-field test: geometric observables constrain the capture sector, while finite-frequency waves probe radial propagation that geometric optics can miss—thereby furnishing a comprehensive, wave-mechanics-based diagnostic of deviations from the Kerr metric and, by extension, from the black-hole uniqueness theorems.

ACKNOWLEDGMENTS

This work is supported by the National Natural Science Foundation of China (NSFC) under Grant nos. 12275106, 12235019 and Shandong Provincial Natural Science Foundation under grant No. ZR2024QA032.

A Additional Numerical Results

This appendix collects the numerical curves referenced in the main text but not displayed there: the tortoise-coordinate view of the effective potential, the frequency resolved hierarchy behind the RMS measure, the total spectra behind the relative deviations, and the direct σ^\pm split behind the azimuthal asymmetry. It also shows the positive amplification form of the superradiant mode discussed in Sec. V.C.

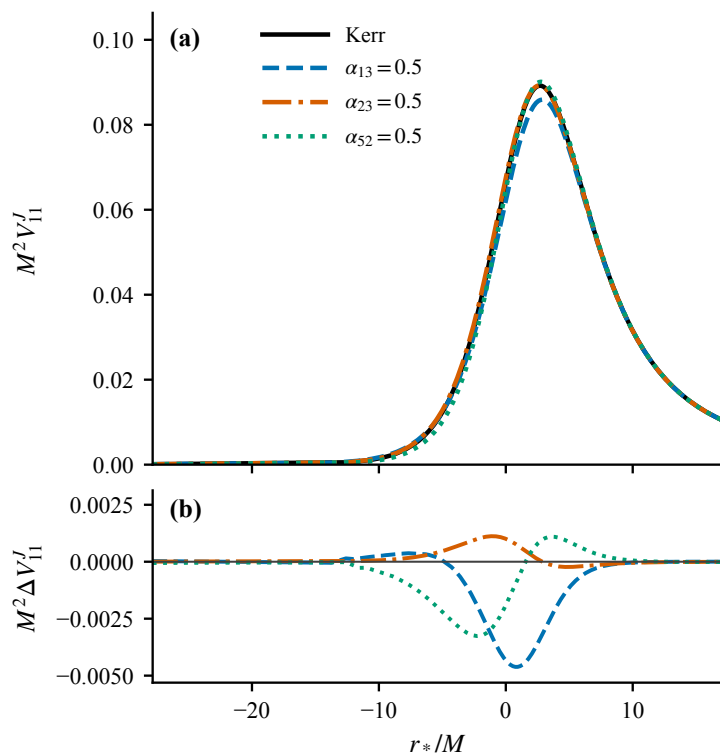


Figure 8: Dimensionless scalar wave effective potential $M^2 V_{11}^J$ plotted against the tortoise coordinate r_*/M for the same parameter choices as Fig. 1: $a/M = 0.6$, $M\omega = 0.3$, and $(l, m) = (1, 1)$. The lower panel shows the difference from Kerr after interpolation onto a common r_*/M grid.

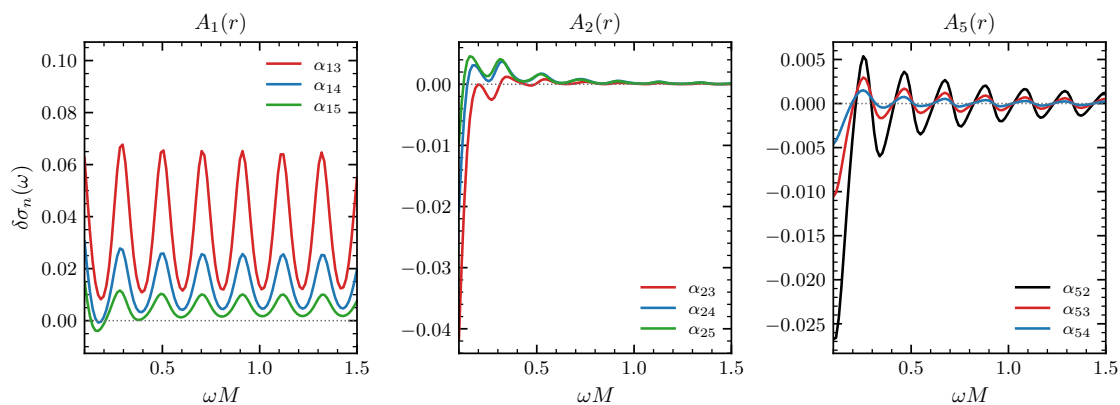


Figure 9: Frequency dependence of the relative deviations used in the hierarchy comparison at $a/M = 0.9$. The three panels correspond to the A_1 , A_2 , and A_5 sectors and show how the signed deviations vary before they are compressed into the RMS quantity S_n in Fig. 3.

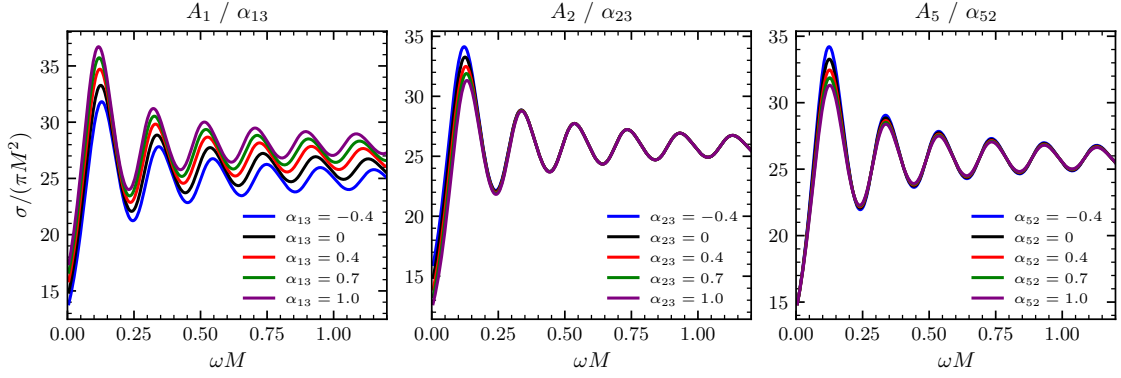


Figure 10: Total absorption spectra for the same on-axis setup as Fig. 5. The curves give the absolute cross sections from which the relative deviations are formed and make the common Kerr envelope visible before normalization.

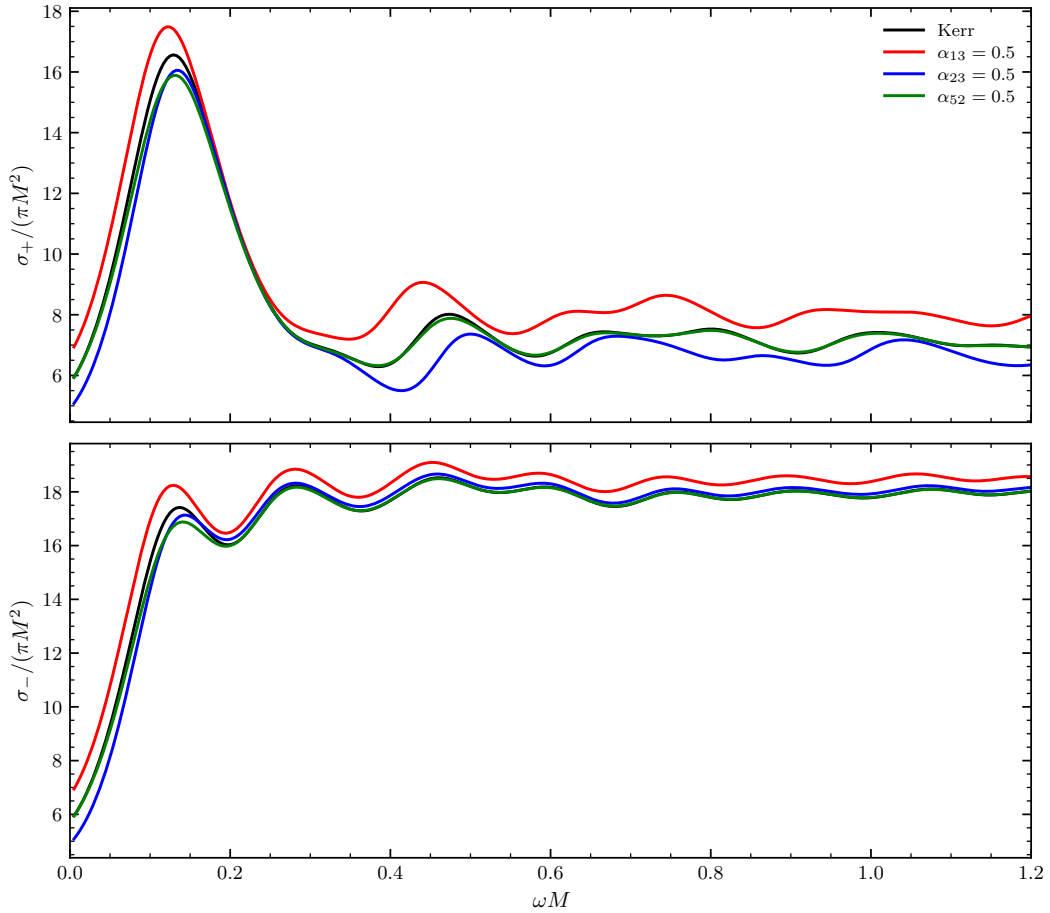


Figure 11: Co- and counter-rotating azimuthal contributions to the absorption spectrum for the off-axis incidence case used in Fig. 6. The split shows the separate σ^+ and σ^- curves whose imbalance defines $\mathcal{A}(\omega)$.

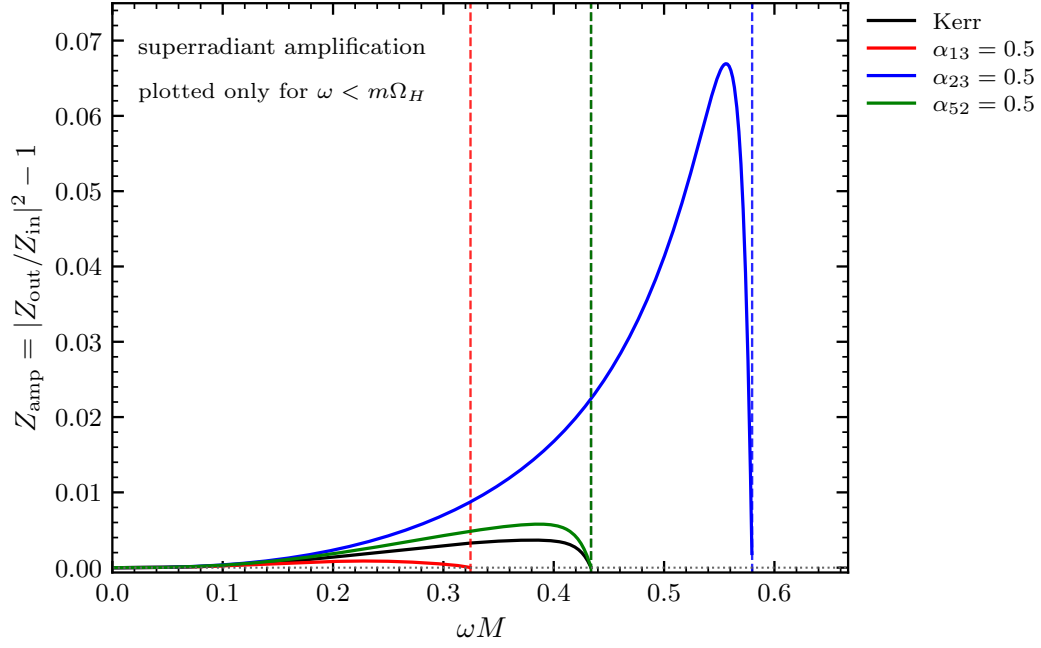


Figure 12: Positive amplification factor of the $l = m = 1$ superradiant mode at $a/M = 0.99$, matching the spin used in Fig. 7. The plotted quantity is $Z_{\text{amp}} = |A_{\text{out}}/A_{\text{in}}|^2 - 1 = -\Gamma_{\omega 11}$ inside the superradiant interval. Vertical dashed lines mark $\omega = m\Omega_H$ for each metric.

References

- [1] Roy P. Kerr. Gravitational field of a spinning mass as an example of algebraically special metrics. *Physical Review Letters*, 11(5):237–238, 1963. doi: 10.1103/PhysRevLett.11.237.
- [2] Brandon Carter. Global structure of the kerr family of gravitational fields. *Physical Review*, 174(5):1559–1571, 1968. doi: 10.1103/PhysRev.174.1559.
- [3] LIGO Scientific Collaboration and Virgo Collaboration, B. P. Abbott, et al. Tests of general relativity with gw150914. *Physical Review Letters*, 116(22):221101, 2016. doi: 10.1103/PhysRevLett.116.221101.
- [4] Event Horizon Telescope Collaboration, Kazunori Akiyama, et al. First m87 event horizon telescope results. i. the shadow of the supermassive black hole. *The Astrophysical Journal Letters*, 875(1):L1, 2019. doi: 10.3847/2041-8213/ab0ec7.
- [5] Leor Barack, Vitor Cardoso, Samaya Nissanke, Thomas P. Sotiriou, et al. Black holes, gravitational waves and fundamental physics: a roadmap. *Classical and Quantum Gravity*, 36(14):143001, 2019. doi: 10.1088/1361-6382/ab0587.
- [6] Charles W. Misner, Kip S. Thorne, and John Archibald Wheeler. *Gravitation*. W. H. Freeman, San Francisco, 1973.
- [7] Robert M. Wald. *General Relativity*. University of Chicago Press, Chicago, 1984.
- [8] Subrahmanyan Chandrasekhar. *The Mathematical Theory of Black Holes*. Oxford University Press, Oxford, 1983.
- [9] Sean M. Carroll. *Spacetime and Geometry: An Introduction to General Relativity*. Addison Wesley, San Francisco, 2004.
- [10] Tim Johannsen and Dimitrios Psaltis. Metric for rapidly spinning black holes suitable for strong-field tests of the no-hair theorem. *Physical Review D*, 83(12):124015, 2011. doi: 10.1103/PhysRevD.83.124015.
- [11] Vitor Cardoso, Paolo Pani, and João Rico. On generic parametrizations of spinning black-hole geometries. *Physical Review D*, 89(6):064007, 2014. doi: 10.1103/PhysRevD.89.064007.
- [12] Tim Johannsen. Regular black hole metric with three constants of motion. *Physical Review D*, 88(4):044002, 2013. doi: 10.1103/PhysRevD.88.044002.
- [13] Zack Carson and Kent Yagi. Asymptotically flat, parametrized black hole metric preserving kerr symmetries. *Physical Review D*, 101(8):084030, 2020. doi: 10.1103/PhysRevD.101.084030.
- [14] Valeri P. Frolov, Pavel Krtous, and David Kubiznak. Black holes, hidden symmetries, and complete integrability. *Living Reviews in Relativity*, 20(1):6, 2017. doi: 10.1007/s41114-017-0009-9.

- [15] R. A. Konoplya, Z. Stuchlík, and A. Zhidenko. Axisymmetric black holes allowing for separation of variables in the klein-gordon and hamilton-jacobi equations. *Physical Review D*, 97(8):084044, 2018. doi: 10.1103/PhysRevD.97.084044.
- [16] Che-Yu Chen and Pisin Chen. Separability of the klein-gordon equation for rotating spacetimes obtained from newman-janis algorithm. *Physical Review D*, 100(10):104054, 2019. doi: 10.1103/PhysRevD.100.104054.
- [17] Rajibul Shaikh. Black hole shadow in a general rotating spacetime obtained through newman-janis algorithm. *Physical Review D*, 100(2):024028, 2019. doi: 10.1103/PhysRevD.100.024028.
- [18] Fen Long, Songbai Chen, Mingzhi Wang, and Jiliang Jing. Shadow of a disformal kerr black hole in quadratic degenerate higher-order scalar-tensor theories. *The European Physical Journal C*, 80(12):1180, 2020. doi: 10.1140/epjc/s10052-020-08744-8.
- [19] Volker Perlick and Oleg Yu. Tsupko. Calculating black hole shadows: Review of analytical studies. *Physics Reports*, 947:1–39, 2022. doi: 10.1016/j.physrep.2021.10.004.
- [20] Kun Meng, Xi-Long Fan, Song Li, Wen-Biao Han, and Hongsheng Zhang. Dynamics of null particles and shadow for general rotating black hole. *Journal of High Energy Physics*, 2023 (11):141, 2023. doi: 10.1007/JHEP11(2023)141.
- [21] W. G. Unruh. Absorption cross section of small black holes. *Physical Review D*, 14(12):3251–3259, 1976. doi: 10.1103/PhysRevD.14.3251.
- [22] Don N. Page. Particle emission rates from a black hole. ii. massless particles from a rotating hole. *Physical Review D*, 14(12):3260–3273, 1976. doi: 10.1103/PhysRevD.14.3260.
- [23] Norma Sanchez. Absorption and emission spectra of a schwarzschild black hole. *Physical Review D*, 18(4):1030–1036, 1978. doi: 10.1103/PhysRevD.18.1030.
- [24] Saul A. Teukolsky. Perturbations of a rotating black hole. i. fundamental equations for gravitational, electromagnetic, and neutrino-field perturbations. *The Astrophysical Journal*, 185:635–647, 1973. doi: 10.1086/152444.
- [25] A. A. Starobinsky and S. M. Churilov. Amplification of electromagnetic and gravitational waves scattered by a rotating “black hole”. *Soviet Physics JETP*, 38:1–5, 1974. Zh. Eksp. Teor. Fiz. 65, 3 (1973).
- [26] S. A. Teukolsky and W. H. Press. Perturbations of a rotating black hole. iii. interaction of the hole with gravitational and electromagnetic radiation. *The Astrophysical Journal*, 193:443–461, 1974. doi: 10.1086/153180.
- [27] J. A. H. Futterman, F. A. Handler, and R. A. Matzner. *Scattering from Black Holes*. Cambridge University Press, Cambridge, 1988.
- [28] Caio F. B. Macedo, Luiz C. S. Leite, Ednilton S. Oliveira, Sam R. Dolan, and Luís C. B. Crispino. Absorption of planar massless scalar waves by kerr black holes. *Physical Review D*, 88(6):064033, 2013. doi: 10.1103/PhysRevD.88.064033.

- [29] Sam R. Dolan. Scattering and absorption of gravitational plane waves by rotating black holes. *Classical and Quantum Gravity*, 25(23):235002, 2008. doi: 10.1088/0264-9381/25/23/235002.
- [30] Luiz C. S. Leite, Sam R. Dolan, and Luís C. B. Crispino. Absorption of electromagnetic and gravitational waves by kerr black holes. *Physics Letters B*, 774:130–134, 2017. doi: 10.1016/j.physletb.2017.09.048.
- [31] Luiz C. S. Leite, Sam R. Dolan, and Luís C. B. Crispino. Scattering of massless bosonic fields by kerr black holes: On-axis incidence. *Physical Review D*, 100(8):084025, 2019. doi: 10.1103/PhysRevD.100.084025.
- [32] Sumit R. Das, Gary Gibbons, and Samir D. Mathur. Universality of low energy absorption cross sections for black holes. *Physical Review Letters*, 78(3):417–419, 1997. doi: 10.1103/PhysRevLett.78.417.
- [33] Atsushi Higuchi. Low-frequency scalar absorption cross sections for stationary black holes. *Classical and Quantum Gravity*, 18(20):L139–L144, 2001. doi: 10.1088/0264-9381/18/20/102.
- [34] Atsushi Higuchi. Addendum to ‘low-frequency scalar absorption cross sections for stationary black holes’. *Classical and Quantum Gravity*, 19(3):599–600, 2002. doi: 10.1088/0264-9381/19/3/401.
- [35] Yves Décanini, Antoine Folacci, and Bruce Jensen. Complex angular momentum in black hole physics and quasinormal modes. *Physical Review D*, 67(12):124017, 2003. doi: 10.1103/PhysRevD.67.124017.
- [36] Yves Décanini, Gilles Esposito-Farèse, and Antoine Folacci. Universality of high-energy absorption cross sections for black holes. *Physical Review D*, 83(4):044032, 2011. doi: 10.1103/PhysRevD.83.044032.
- [37] Yves Décanini, Antoine Folacci, and Bernard Raffaelli. Fine structure of high-energy absorption cross sections for black holes. *Classical and Quantum Gravity*, 28(17):175021, 2011. doi: 10.1088/0264-9381/28/17/175021.
- [38] Carolina L. Benone, Luiz C. S. Leite, Luís C. B. Crispino, and Sam R. Dolan. On-axis scalar absorption cross section of kerr-newman black holes: Geodesic analysis, sinc and low-frequency approximations. *International Journal of Modern Physics D*, 27(11):1843012, 2018. doi: 10.1142/S0218271818430125.
- [39] Mohamed Ould El Hadj. Black hole absorption cross sections: Spin and regge poles. *Physical Review D*, 111(12):124041, 2025. doi: 10.1103/vj91-h7wd.
- [40] Luiz C. S. Leite, Carolina L. Benone, and Luís C. B. Crispino. Scalar absorption by charged rotating black holes. *Physical Review D*, 96(4):044043, 2017. doi: 10.1103/PhysRevD.96.044043.
- [41] Caio F. B. Macedo and Luís C. B. Crispino. Absorption of planar massless scalar waves by bardeen regular black holes. *Physical Review D*, 90(6):064001, 2014. doi: 10.1103/PhysRevD.90.064001.

- [42] E. S. de Oliveira. Scalar absorption cross section of rotating black holes with tidal charge. *Physical Review D*, 104(12):124008, 2021. doi: 10.1103/PhysRevD.104.124008.
- [43] Yang Li and Yan-Gang Miao. Absorption cross section of regular black holes in scalar-tensor conformal gravity. *Physical Review D*, 105(4):044031, 2022. doi: 10.1103/PhysRevD.105.044031.
- [44] Marco A. A. De Paula, Luiz C. S. Leite, Sam R. Dolan, and Luís C. B. Crispino. Absorption and unbounded superradiance in a static regular black hole spacetime. *Physical Review D*, 109(6):064053, 2024. doi: 10.1103/PhysRevD.109.064053.
- [45] Yang Huang and Hongsheng Zhang. Scattering of massless scalar field by charged dilatonic black holes. *The European Physical Journal C*, 80:654, 2020. doi: 10.1140/epjc/s10052-020-8228-8.
- [46] Jining Tang, Yang Huang, and Hongsheng Zhang. Absorption and scattering of massless scalar waves by frolov black holes. *Physical Review D*, 113:084031, 2026. doi: 10.1103/PhysRevD.113.084031.
- [47] F. de Felice and G. Preti. On the meaning of the separation constant in the kerr metric. *Classical and Quantum Gravity*, 16(9):2929–2935, 1999.
- [48] E. T. Newman, E. Couch, K. Chinnapared, A. Exton, A. Prakash, and R. Torrence. Metric of a rotating, charged mass. *Journal of Mathematical Physics*, 6(6):918–919, 1965. doi: 10.1063/1.1704351.
- [49] R. A. Konoplya and A. Zhidenko. Detection of gravitational waves from black holes: Is there a window for alternative theories? *Physics Letters B*, 756:350–353, 2016. doi: 10.1016/j.physletb.2016.03.044.
- [50] Ashoke Sen. Rotating charged black hole solution in heterotic string theory. *Physical Review Letters*, 69(7):1006–1009, 1992. doi: 10.1103/PhysRevLett.69.1006.
- [51] Sarah Vigeland, Nicolas Yunes, and Leo C. Stein. Bumpy black holes in alternate theories of gravity. *Physical Review D*, 83(10):104027, 2011. doi: 10.1103/PhysRevD.83.104027.
- [52] Nicolas Yunes and Leo C. Stein. Non-spinning black holes in alternative theories of gravity. *Physical Review D*, 83(10):104002, 2011. doi: 10.1103/PhysRevD.83.104002.
- [53] Nicolas Yunes and Frans Pretorius. Dynamical Chern–Simons modified gravity. i. spinning black holes in the slow-rotation approximation. *Physical Review D*, 79(8):084043, 2009. doi: 10.1103/PhysRevD.79.084043.
- [54] A. N. Aliev and A. E. Gümrükçüoğlu. Charged rotating black holes on a 3-Brane. *Physical Review D*, 71(10):104027, 2005. doi: 10.1103/PhysRevD.71.104027.
- [55] Clifford M. Will and Jr. Nordtvedt, Kenneth. Conservation laws and preferred frames in relativistic gravity. i. preferred-frame theories and an extended ppn formalism. *The Astrophysical Journal*, 177:757–774, 1972.

- [56] Clifford M. Will. The confrontation between general relativity and experiment. *Living Reviews in Relativity*, 17:4, 2014. doi: 10.12942/lrr-2014-4.
- [57] Clifford M. Will. *Theory and Experiment in Gravitational Physics*. Cambridge University Press, Cambridge, 2 edition, 2018.
- [58] Carson Flammer. *Spheroidal Wave Functions*. Stanford University Press, Stanford, 1957.